Chemical Engineering Journal 428 (2022) 131142

Contents lists available at ScienceDirect

Chemical Engineering Journal

journal homepage: www.elsevier.com/locate/cej

Breathable and superhydrophobic photothermic fabric enables efficient interface energy management via confined heating strategy for sustainable seawater evaporation

Chang Zhang [a,b], Peng Xiao [a,b,*], Feng Ni [a,b], Jincui Gu [a,b], Jianhua Chen [c], Yujing Nie [c], Shiao-Wei Kuo [d], Tao Chen [a,b,*]

[a] Key Laboratory of Marine Materials and Related Technologies, Zhejiang Key Laboratory of Marine Materials and Protective Technologies, Ningbo Institute of Material Technology and Engineering, Chinese Academy of Sciences, Zhongguan West Road 1219, 315201 Ningbo, China
[b] School of Chemical Sciences, University of Chinese Academy of Science, Beijing 100049, China
[c] College of Chemistry, Chemical Engineering and Environment, Minnan Normal University, Zhangzhou 363000, China
[d] Department of Material and Optoelectronic Science, Center of Crystal Research, National Sun Yat-Sen University, Kaohsiung 804, Taiwan

ARTICLE INFO

Keywords:
Confined heating
Salt rejection
Seawater desalination
Breathable
Photothermal fabric

ABSTRACT

Achieving solar-heating-enabled sustainable water purification from seawater is considered a promising strategy for alleviating the water crisis worldwide. Since preventing salt contamination becomes a crucial consideration in practical application, extensive efforts have been devoted in recent years. However, there has been an urgent push to realize both efficient and stable seawater evaporation in a simple and scalable way. Here, we present a solar-enabled confined heating strategy to efficiently purify seawater, in which system the self-closed "cover" is composed of breathable, photothermal, and superhydrophobic fabric (PSHF). The confined heating strategy can remarkably reduce heat conduction loss during the evaporation process via an effective energy management. Note that when the thickness of the evaporator is optimized to 4 mm, the heat conduction can reduce to 0.98%, and the total heat loss is only 7.1%. As a result, the evaporation rate can be reach up to 1.49 kg/m^2/h with the evaporation efficiency of 91.68% under 1 sun irradiation. The superhydrophobic properties of the photothermal layer can also endow the evaporators with good salt rejection performance. In our system, the PSHF can significantly endure salt pollution and remain stable under long-term evaporation of 12 h. Furthermore, this system can also maintain long-term salt-rejecting stability for evaporation sustainability, demonstrating significant potentials in stable and efficient seawater purification.

1. Introduction

Desalination of seawater is a feasible strategy that can alleviate the water crisis worldwide.[1,2] The implement of solar energy input to purify seawater is expected to be a promising and sustainable approach considering the energy consumption and climate problem of global warming.[3–7] Recently, the rising solar-heating interfacial evaporation system can efficiently convert solar light to thermal energy to heat the air–water interface.[8–12] In this system, (1) strengthening the solar-to-thermal conversion efficiency of absorbers,[13–15] (2) minimizing heating loss,[16–18] (3) optimizing the water channel[19–21] and (4) rejecting salt blockage[22–24] are four key factors related to the materials and devices for sustainable and efficient purified water collection. Based on this, extensive efforts have been dedicated to synthesize a variety of photothermal structured materials and design versatile evaporators to elevate the evaporation rate and block salt contamination.[7,25–28] Specifically, the salt aggregate in the solar evaporation process accounts for unsustainable clean water generation, which can severely hinder the water transportation channel and weaken solar absorption. Thus, there has been a push to develop viable strategies to solve this problem. Some typical solutions are presented to alleviate or prevent the problem of salt contamination.[29] Generally, two main working mechanisms have been employed, including contact interface and contactless one. In the contact system, there are some specific design

* Corresponding authors at: Key Laboratory of Marine Materials and Related Technologies, Zhejiang Key Laboratory of Marine Materials and Protective Technologies, Ningbo Institute of Material Technology and Engineering, Chinese Academy of Sciences, Zhongguan West Road 1219, 315201 Ningbo, China (P. Xiao).
E-mail addresses: xiaopeng@nimte.ac.cn (P. Xiao), tao.chen@nimte.ac.cn (T. Chen).

https://doi.org/10.1016/j.cej.2021.131142
Received 10 April 2021; Received in revised form 7 June 2021; Accepted 30 June 2021
Available online 6 July 2021

such as Janus structured absorbers,[30–33] superhydrophobic floating evaporators,[34–37] biomimetic three-dimensional (3D) printing with localized crystallization,[38] wicking effect,[39] Marangoni effect-driven salt rejection,[40] edge-preferential salt crystallization,[41] hanging structures,[42] etc. For the contactless one, the considerable thermal radiation can indirectly heat the bulk water surface via construction of programmed evaporators.

Although various solar absorbers or evaporation prototypes have focused on stable and durable seawater purification, further efficiency improvement of the evaporators with good salt rejection still needs to be solved due to the potential energy loss such as heat convection, heat radiation, and heat conduction. In previous studies, the evaporator can achieve stable salt-rejecting evaporation, but the solar energy conversion efficiency is relatively low.[30,33,43,44] In addition, there are still many problems in the design of the solar-driven evaporators, such as difficulty in large-scale preparation,[45–47] complexity in the fabrication process,[48,49] and the high cost[50,51]. Therefore, it remains a great challenge to simultaneously achieve high energy conversion efficiency and stable salt-rejecting in a facile and low-cost way.

Herein, we fabricate photothermal and superhydrophobic fabrics (PSHF) which can be produced on a large scale by a completely wet manufacturing strategy. The prepared PSHF has breathable and photothermal conversion properties. At the same time, because of the superhydrophobic properties, it can reject the brine under long-term solar irradiation and can keep a relatively stable evaporation performance in brine. Furthermore, we designed a confined heating structure to achieve high-efficiency seawater purification. The prepared PSHF was loaded on the confined heating evaporator. This confined heating evaporator can achieve energy management by reducing heat conduction losses during the evaporation process. Note that when the thickness of the evaporator is optimized to 4 mm, the heat conduction can reduce to 0.98%, and the total heat loss is only 7.1%. The evaporation rate can be optimized to 1.49 kg/m^2/h, and the evaporation efficiency is 91.68% under 1 sun irradiation (1 kW/m^2). Compared with the conventional evaporator, the evaporation efficiency can only reach 33.76%, and the efficiency is 57.92% higher. The superhydrophobic properties of the photothermal layer can also endow the evaporators with excellent salt-rejecting performance. It can remain stable under the long-term evaporation of 12 h. This system shows great potential for stable and efficient seawater purification.

2. Materials and methods

2.1. Materials

The pure fabric was purchased from the Bulilai company, and its main ingredient is polyester. Ferric chloride ($FeCl_3{\cdot}6H_2O$), pyrrole monomer, Polydimethylsiloxane (PDMS), and PFDTS ($C_{16}H_{19}F_{17}O_3Si$) were purchased from Aladdin.

2.2. Preparation of PSHF

The pure fabric was first soaked in ethanol to wash away excess impurities in the fabric. After drying, it was immersed in the pure pyrrole monomer solution. After the fabric was full of pyrrole monomer, it was soaked pyrrole monomer/fabric in 0.1 mol/L $FeCl_3$ solution for polymerization at room temperature for 1 h. After the polymerization was completed, then it was rinsed the excess ferric chloride on the surface with water and placed in the oven for 2 h (100 °C) to obtain polypyrrole fabric (PPy-Fabric). After that PPy-Fabric was immersed in PFDTS/toluene solution (3 wt%), and heated and reacted for 2 h. After successfully modified by PFDTS, the photothermal superhydrophobic fabric (PSHF) was obtained.

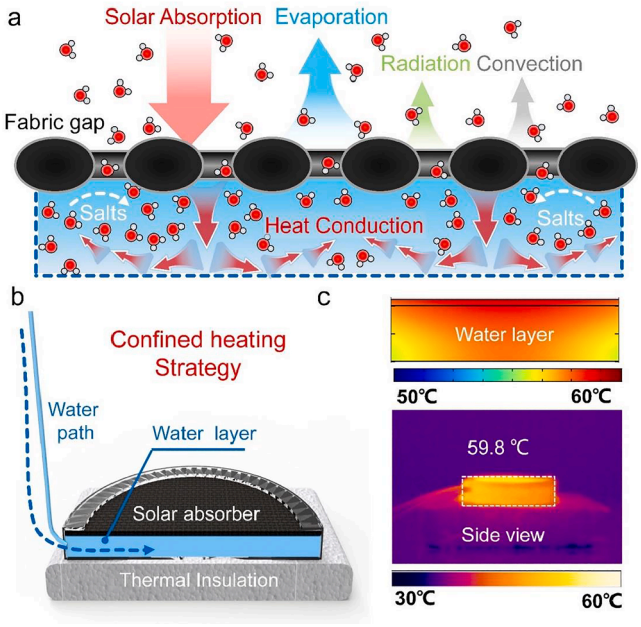

Fig. 1. (a) Sketch of confined heating strategy. (b) Sketch of space confinement heating device. (c) Simulation's image and IR image of the confined heating device under solar irradiation.

2.3. Preparation of confined heating device with different thickness

The PSHF was cut into a circle with a diameter of 33 mm. Then, it was attached to a plastic disc as a self-closed 'cover'. A thin rubber hose was attached to the side of the plastic disc to transport the water. Finally, the bottom of the plastic disc was covered with a silicone plate of appropriate size, and PDMS was used for packaging to ensure that all connections do not leak.

2.4. Solar-driven water purification experiment in laboratory

The resulted solar-driven purification devices were set under the irradiation of Solar Simulator (HM-Xe500W) equipped with an AM 1.5 G filter for water purification. The mass change (m) of water during evaporation was recorded using an electronic scale. In the experiment, the simulated seawater is NaCl solution (3.5%) solution.

2.5. Outdoor experiment for solar-driven water purification experiment

The confined heating evaporation device with a diameter of 5 mm PSHF was placed in a transparent PMMA water collection box. The simulation seawater storage bottle was put outside the box and connected the evaporator in the box through a thin tube. The real sea water from the South China Sea was used in this experiment. The whole evaporation and water collection device was exposed under the true sunlight irradiation to collect water for 12 h. After evaporation and collection, the mass of the fresh water was weighed. A light intensity machine (Precisa PL-132) was used to record the hourly sunlight intensity.

2.6. Characterizations

Field emission scanning electron microscope (FE-SEM) with a FE scanning electron microanalyzer (Hitachi-S4800, 8 kV) was used to observe the morphologies and microstructures of and PSHF respectively. The chemical composition and elemental maps of samples were measured by energy dispersive X-ray spectroscopy (EDS, Thermo scientific, USA). X-ray photoelectron spectroscopy (XPS) analysis is

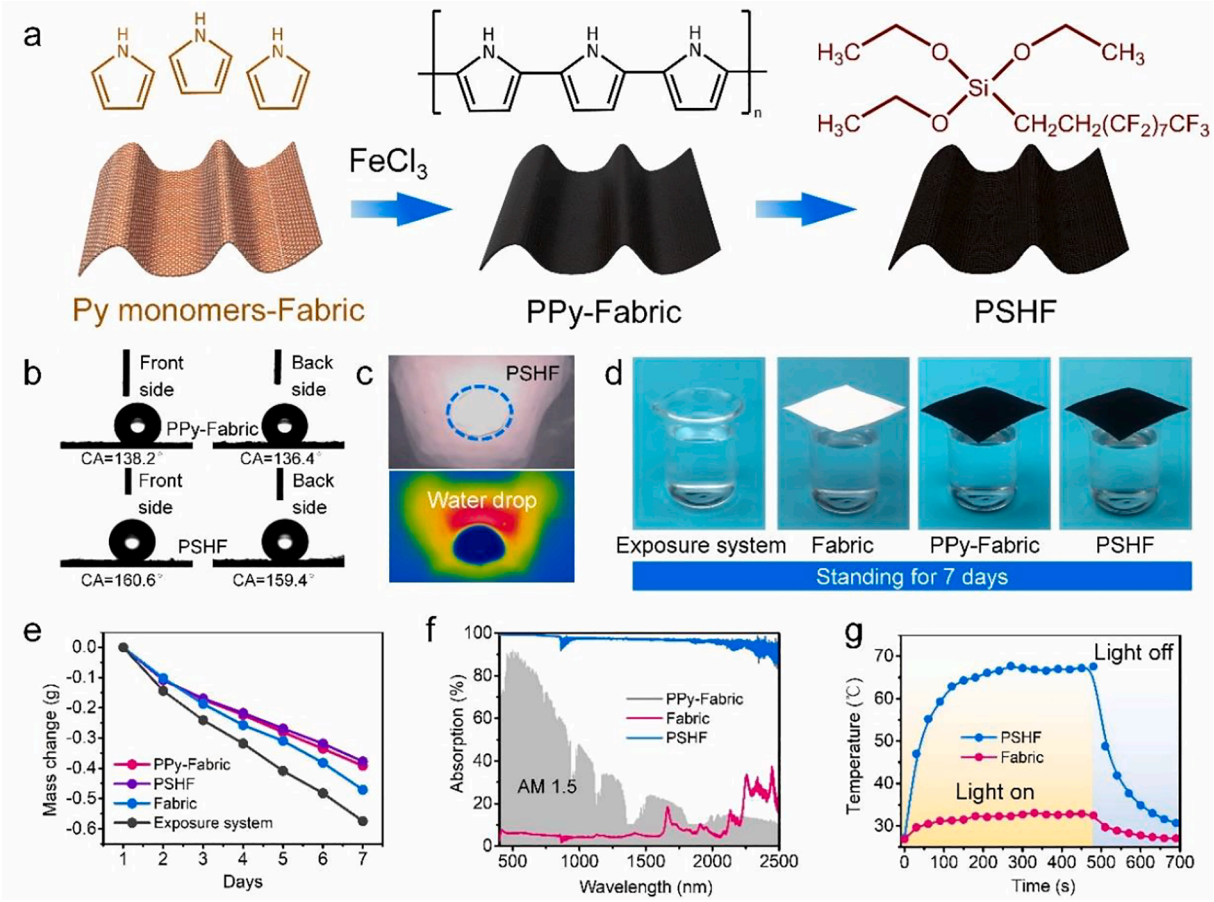

Fig. 2. (a) The fabricating process of PSHF. (b) The contact angles for both sides of PPy-Fabric and PSHF. (c) Super-repellency to water drop under solar irradiation. (d) Breathable test of Fabric, PPy-Fabric, PSHF and bulk water for 7 days. (e) Mass change versus time curves of different material in breathing test. (f) The UV-absorption spectra of different samples in the wavelength range of 400 to 2500 nm and comparison with the standard AM 1.5G spectrum filter. (g) Temperature versus time curves of PSHF and Fabric.

performed on a Shimadzu Axis Ultradld spectroscope, using C-O (alpha) as radiation resource. The contact angle of water droplets and underwater bubbles on surfaces was carried out by a contact angle meter (DCAT21), using a 3 μL and 5 μL droplet as an indicator. IR thermal images and the corresponding temperatures were captured using the IR thermal camera (Optris PI 400). The concentrations of ions in the water were analyzed by inductively coupled plasma atomic emission spectroscopy (ICP-AES, NexION 300X). The absorption spectra of samples were performed using an ultraviolet–visible–near-infrared spectrophotometer equipped with an integrating sphere (Lambda 950). The thermal conductivity of materials was evaluated by Laser Thermal Instruments (LFA457).

3. Results and discussion

As shown in Fig. 1a, this confined heating strategy can significantly improve the energy utilization efficiency during the solar-driven evaporation process by reducing the heat conduction loss. As shown in Fig. 1b, we use such a device to achieve this confined heating strategy. In this system, a photothermal superhydrophobic fabric (PSHF) that we refer to it as a self-closed 'cover' is introduced to heat the confined water layer. And a thin tube is used to transport water into the confined heating evaporator. At the bottom of the confined heating evaporator, PS foam was used as a thermal insulation layer which prevents the heat conduction from diffusing to the outside.Because the water layer in a confined evaporator is thin, the thin water layer can be heated to a higher temperature quickly in a short time. As the temperature division image of the simulated longitudinal thin water layer and the IR image of the confined heating shown in Fig. 1c. It can be concluded that the solar absorber on the surface of the confined heating device can reach 59.8 ℃ rapidly under the irradiation of 1 sun (1 kW/m^2), and the steam can quickly evaporate through the gap of the fabric.

The PSHF used in this work can be produced on a large scale and simply through a fully wet manufacturing strategy, with good air permeability and photothermal conversion performance. Furthermore, a well-designed prototype is achieved to conduct outdoor testing under natural sunlight. The self-closed photothermal cover with confined interface heating is effective and scalable in a simple and rational design strategy, demonstrating a significant effect on sustainable and efficient seawater desalination.

The black PSHF used in this work can be obtained by in-situ growth strategy which can mainly be divided into three steps as revealed in Fig. 2a. Firstly, the ethanol was used to wash away the dust of pure fabric (Fig. S1a and S1d). After ethanol volatilization, this pure fabric was soaked in the pure pyrrole monomer to attach the pyrrole. To endow this fabric with excellent light absorption performance, the oxidation polymerization method is adopted by us. The surface of the fabric can be coated with a dense black polypyrrole layer after oxidation polymerization (Fig. S1b and S1e). Next, PFDTS was used to modify on PPy-Fabric. The PFDTS as a coupling agent can greatly improve the hydrophobicity of the material through decreases the surface energy and provides the essential roughness to achieve superhydrophobic property. [52] After modification, the hierarchical spherical microstructure of PSHF surface was still preserved completely (Fig. S1c, S1f and S2). As shown in Fig. S1g, PSHF can be produced in large scale though this all-wet fabrication strategy.

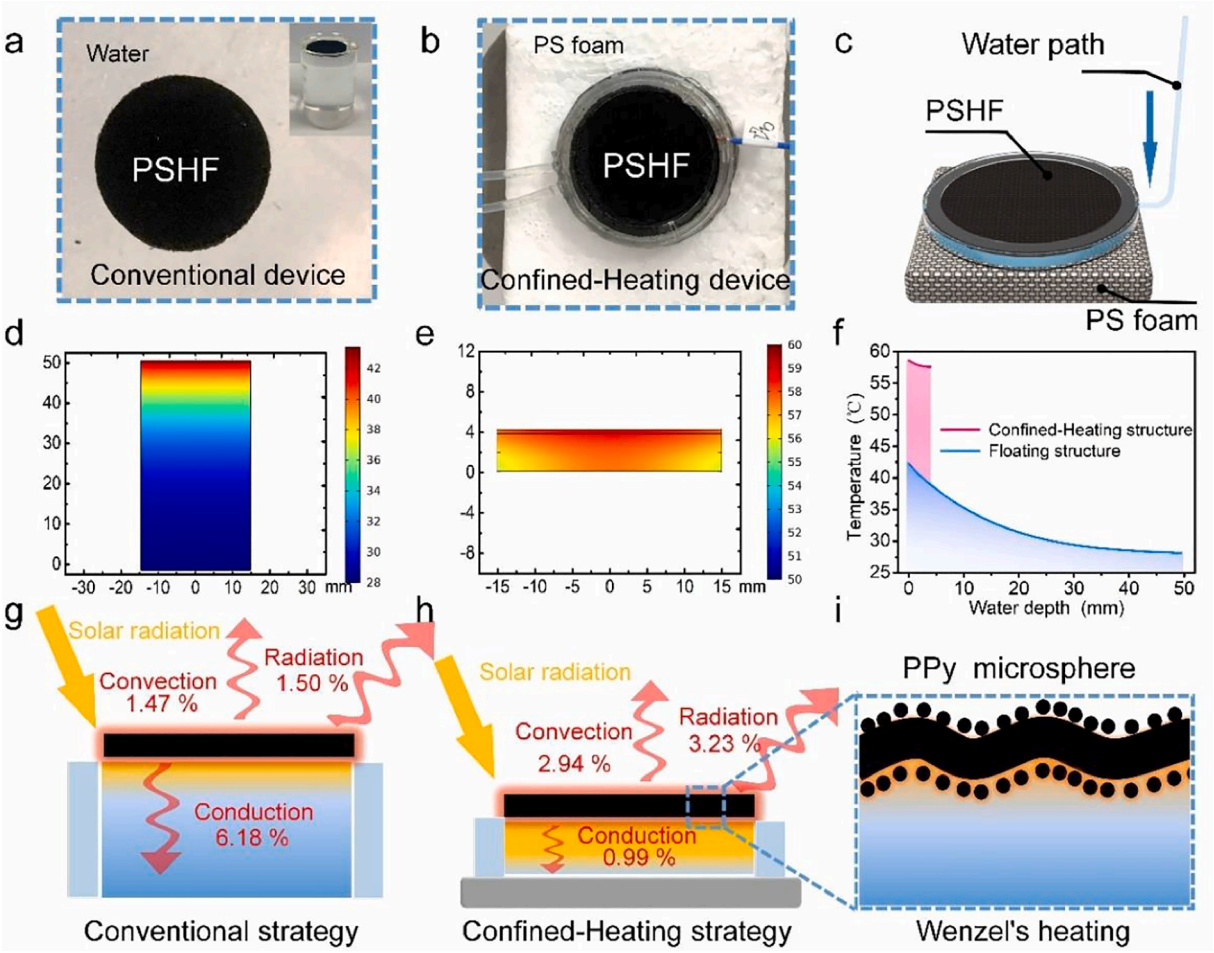

Fig. 3. (a-b) Photograph of conventional strategy and confined heating evaporation strategy. (c) The evaporation mechanism of the confined heating evaporation structure. (d-e) Temperature distribution of conventional strategy and confined heating strategy by COMSOL simulation under 1 sun irradiation. (f) Vertical temperature distribution of the conventional strategy and confined heating strategy by COMSOL simulation. (g-h) The comparison of heat loss model between conventional structure and confined heating structure. (i) Schematic diagram of micro-heating mechanism of the confined heating evaporator.

At the same time, the smaller droplet (3 μL) was also used to press at the PSHF surface. Through the photos, we found that due to the high liquid resistance of the surface, the droplet can be easily lifted after pressing without any changes on the surface (Fig. S3). As shown in Fig. 2b, the contact angles of PPy-Fabric and PSHF show that both sides of surfaces have the same hydrophobic properties. Before modification with PFDTS, the contact angles of PPy-Fabric are 138.2° and 136.4° respectively. After modification, the contact angles of PSHF are 160.4° and 159.4° respectively, which confirms that the modification can convert it to a superhydrophobic surface.

In order to prove the stability of the superhydrophobic property of the surface of PSHF, we tested it under solar irradiation. As shown in Fig. 2c, it can be observed that the water droplet had a distinct boundary with PSHF from the 2D IR image. We also test the time stability of the droplet on the surface of PSHF under 1 sun (1 kW/m^2) solar irradiation. By observing the photo from the side view, it can be found that the PSHF has an obvious non-infiltrating boundary with the droplet. (Fig. S4) Even if the under the irradiation of 1 h, there is no obvious change. Therefore, under strong solar irradiation, the robust superhydrophobic property remains stable and doesn't disappear. This property provides the basis for salt-rejecting performance in solar-driven water evaporation.

Due to the PSHF can't be wetted with water. Different from the surface of the conventional hydrophilic evaporator, water can't flow through the photothermal surface layer during the evaporation process. Therefore, the vapor permeability of the photothermal surface layer is considered to be an important factor affecting the evaporation rate.[53] First of all, we used a simple method to test the vapor permeability of these fabric samples. Compared with the exposure system, three kinds of samples pure fabric, PPy-Fabric, and PSHF were covered tightly on the beaker with the same amount of water (Fig. 2d). As shown in Fig. 2e, after 7 days of observation and recording, except for the great changes in the mass of exposure system, the mass changes of the other three kinds of samples are extraordinarily close. Besides, we also used a vapor transmission apparatus to verified the vapor permeability of pure fabric, PPy-Fabric, and PSHF in a short time systematically (Fig. S5). After 15 h of vapor through experiment, the water vapor through rate of pure fabric, PPy-Fabric, and PSHF are 1082.55 m^3/day, 1056.88 m^3/day and 1043.78 m^3/day, respectively. Therefore, we can conclude that the coverage of polypyrrole and PFDTS rarely affects its vapor permeability of PSHF. During the solar-driven evaporation process, vapor can still quickly pass through the photothermal surface layer composed of breathable PSHF.

Furthermore, the excellent sunlight absorption capacity of photothermal materials can significantly enhance their solar-driven evaporation performance. From the UV–vis-IR absorption spectrum in Fig. 2f, it can be observed that pure fabric has a low light absorption. However, after modified with polypyrrole, the light absorption of PPy-Fabric has about 98% absorption of total solar energy (weighted under AM 1.5G) in the wavelengths from 400 to 2500 nm. Compared with pure fabric, this is a significant improvement. Similarly, the light absorption of PSHF is also about 98%. (The gray line of PPy-Fabric is covered by the blue line

of PSHF due to the imperceptible changes in light absorption before and after modification). Therefore, the modification of PFDTS has little effect on light absorption. In addition, the temperature versus curves of PSHF and pure fabric under 1 sun solar irradiation are also measured in Fig. 2g. The surface temperature of PSHF can rapidly rise to 67.2 °C in 300 s while pure fabric can only rise to 32.7 °C at the same time (room temperature is 27 °C). Fig. S6 shows the IR images of PSHF and pure fabric in this heating process. Compared with pure fabric, PSHF has better photothermal conversion performance.

To explore the chemical composition of these fabric samples, X-ray photoelectron spectroscopy (XPS) and energy dispersion spectrum (EDS) were employed in our work. As shown in Fig. S7 and Fig. S8, there is more F element and Si element PSHF sample than that of PPy-Fabric. As shown in Tab. 1 and Fig S9, compared with PPy-Fabric, the contents of fluorine and silicon in PSHF were significantly increased. Thus, the EDS result illustrates that the PFDTS are successfully introduced into our system. Besides, XPS characterization was also conducted to explore the refined peaks in the surface of PPy-Fabric and PSHF. Three main characteristic peaks appeared in these two samples at the binding energies of 285 eV, 400 eV, and 532 eV belonging to C 1 s, N 1 s, and O 1 s. Besides that, two extra characteristic peaks appeared in PSHF samples at the binding energies of 689 eV and 200 eV belonging to F 1 s and Si 2p (Fig. S10a). Regarding the high-resolution C 1 s spectra, the PSHF displayed three fitting peaks at 284.4 eV (C − C bonds), 285.6 eV (C − N bonds), and 287.5 eV (C = O bonds) (Fig. S10b). Due to the low contents of F element and Si element in PSHF, C-F bond and C-Si bond don't appear in the high-resolution C 1 s spectra. C–C bond and C-O bond are mainly provided by the original fabric, and the C-N bond can prove the polypyrrole has been successfully modified on the original fabric.

The PSHF can be designed as a surface layer of an evaporation device because of its photothermal and superhydrophobic properties. As photos are shown in Fig. 3a, the PSHF has covered the water surface directly as a conventional evaporation device. In a confined heating evaporation device, PSHF is a self-closed 'cover' that is introduced to heat the confined bulk water (Fig. 3b). And Fig. 3c shows the schematic of the confined heating evaporation device. The water layer of limited thickness is confined in a transparent plastic container, and the photothermal conversion layer on the top is the PSHF. The water is transferred to the

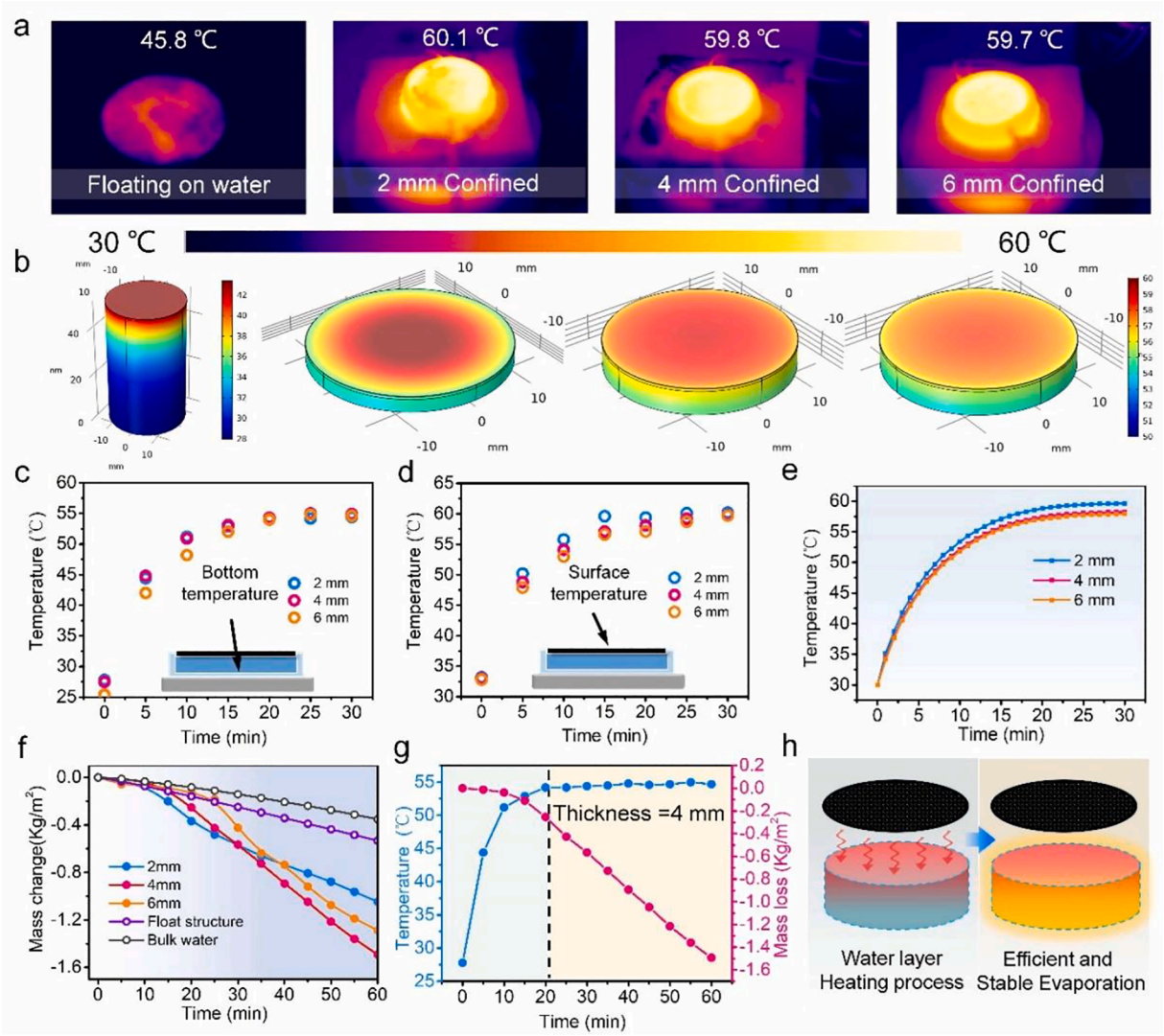

Fig. 4. (a) IR images of 2 mm, 4 mm, 6 mm and floating structure under 1 sun irradiation. (b) Temperature distribution of PSHF when equilibrated with various thicknesses for floating structure 2 mm, 4 mm, 6 mm and by COMSOL simulation under 1 sun irradiation. (c) Bottom temperature versus time curves of 2 mm, 4 mm and 6 mm thickness structure. (d) Surface temperature versus time curves of 2 mm, 4 mm and 6 mm thickness structure. (e) Surface temperature versus time curves of 2 mm, 4 mm and 6 mm thickness structure by COMSOL simulation under 1 sun irradiation. (f) Mass change versus time curves of bulk water and 2 mm, 4 mm, 6 mm, floating structure, and bulk water under 1 sun irradiation. (g-h) Two special evaporation processes (Heating process and Stable process) in a confined heating evaporator.

confined heating evaporator through a thin rubber tube constantly.

To evaluate the temperature division of the two modes in the evaporation process, the vertical temperature distribution of the conventional strategy and confined heating strategy was further simulated by COMSOL Multiphysics in Fig. 3d and Fig. 3e (detailed discussion in Supporting Information). Due to the heat conduction into the bulk water layer constantly in a floating structure, a part of the upper bulk water is heated to a certain temperature after 30 min of solar irradiation.

In this system, a part of the solar energy is used to increase the sensible heat of the bulk water (increase the temperature of the bulk water). However, the temperature distribution of the thin water layer in the confined heating evaporator tended to be stable after 30 min of solar irradiation. In this system, solar energy can be efficiently used to increase latent heat (phase change energy) of water in a thin layer, thus achieving efficient water evaporation. And Fig. 3f shows the vertical temperature distribution curve for 30 min under 1 sun irradiation. Compared with the water layer temperature of conventional structure surface which can be heated to about 45.2 °C, the confined evaporator can be heated to about 60.1 °C in a short time, which provides the basis for it to achieve rapid evaporation.

In addition, we also calculated the heat loss of these two systems. As shown in Fig. 3g and 3 h, these are two schematic diagrams of the conventional heat loss model and the confined heating heat loss model. The water supply in a conventional system is through sucking water from bulk water by capillary force, which will keep the system in a water-saturated state. Thus, much energy could be lost by the system. Through the heat loss calculation of this conventional evaporation strategy, it can be calculated that the heat convection is 1.47% and radiation is 1.52%, and heat conduction is 7.1% (The thickness of evaporator is 4 mm). However, in the confined heating evaporator. This system can cut off the connection between the evaporation device and bulk water, thus there is hardly energy dissipation into bulk water. At the same time, the downward heat conduction restricted to the fixed thickness of the water layer will be isolated by the PS foam. Through the heat loss calculation of confined heating evaporation strategy, it can be calculated that the heat convection is 2.92% and radiation is 3.20%, and heat conduction is 0.98%. Specific heat conduction and heat loss calculation methods can be obtained in the supporting material. Through two kinds of systems of heat loss calculation results, we can conclude that the confined heating type evaporator is much less than the conventional floating evaporative device heat conduction loss. However, in the heat convection and radiation part, the cause of this part is higher than the conventional floating evaporative device due to confined heating evaporator can achieve higher surface temperature.

As shown in Fig. S11a-c, there are three kinds of wetting models respectively. First, in Young's model, the γ is defined as the contact angle of the liquid on the solid surface. On the superhydrophobic solid surface, Wenzel's model, and Cassie–Baxter's model are two different infiltration modes respectively.[54,55] Wenzel's model usually has a large rolling angle due to the close contact of droplets with a solid surface. On the contrary, the Cassie–Baxter's model usually has a smaller rolling angle (Fig. S11d and S11e).[56]

When the PPy and PFDTS were modified on fabric successfully, the contact angle reached a constant value of ≈ 158°. Furthermore, although the PSHF has highly hydrophobic, exhibited high adhesion to water droplets. As shown in Fig. S11f, when the fabric turned to about 50.8°, the water droplets still firmly adhered to the surface. This wettability with high water contact angle as well as high adhesion to water droplets of the hydrophobic fabric is regarded as Wenzel's wetting behavior, under which, although substrate surface exhibits a high contact angle, water can penetrate the rough surface structures of the substrate and displace the otherwise air pockets present under Cassie's wetting (Fig. 3i). This Wenzel's wetting behavior of the fabric is a result of the combination of both the micro-sized surface structure and the hydrophobic modification. Under Wenzel's wetting state, contact between the water and solid substrate surface is intimate and maximized, which is beneficial for the heat transfer from the fabric to water as air otherwise is considered as a poor heat conductor.[57]

We used an IR camera to observe and record the temperature rise curve and photos of the conventional floating evaporation device under 1 sun (Fig. S12). As a result, the surface temperature of this device can only reach about 45.2 °C for a short time rather than rise further. However, the confined heating evaporator has the characteristic of heating a thin water layer, so the water can be heated to a higher temperature to achieve a higher evaporation rate. Hence, the thickness of the water layer may be an important factor to consider to affect the evaporation rate of the confined heating evaporator. Different thicknesses of confined heating evaporators were designed and fabricated in 2 mm, 4 mm, and 6 mm. At the same time, we also took 2D infrared photos of 2 mm, 4 mm, and 6 mm evaporators that stabilized after 30 min. The highest surface temperatures were 60.1 °C, 59.8 °C, and 59.7 °C respectively (Figs. S13 and 4a). And the heat loss of these three evaporators is shown in Tab. 2. The calculation results show that the heat loss will increase with thickness. However, because the confined evaporator has a higher surface temperature, the heat convection and radiation loss will be slightly higher than that of the conventional evaporator. In addition, the experiment result was further simulated by COMSOL Multiphysics, which were highly coincided with the above-mentioned tendency (Fig. 4b and Fig. S14) (detailed discussion in Supporting Information). It can be concluded that there is no obvious change in the final stable temperature for different thicknesses of the water layer.

As shown in Fig. 4c, we used a temperature detector to measure the real-time temperature at the water layer bottom for 0 to 30 min. As a result, the heating rates of the confined heating evaporator with 2 mm and 4 mm water layer thickness are relatively close. And the evaporator with a layer thickness of 6 mm is slower. As shown in Fig. 4d, the IR image was employed to monitor the surface temperature of different water layer thicknesses for 0 to 30 min. The measurement results show that the heating rates of the confined heating evaporator with 4 mm and 6 mm water layer thickness are relatively close. And an evaporator with a thickness of 2 mm is faster. In addition, the experiment result was also simulated by COMSOL Multiphysics, which were also coincided with the above-mentioned tendency (Fig. 4e) (detailed discussion in Supporting Information).

In addition, the mass changes of PSHF with a series of water layer thickness overtime under 1 sun are also recorded in Fig. 4f. Superior to bulk water and floating structure, the PSHF with a series of water layer thickness demonstrates higher mass loss. The solar-driven evaporation rate and efficiency are two crucial parameters for evaluating the capability of a solar vapor generation system (Fig. S15). The following two formulas are used to calculate the evaporation rate and evaporation efficiency respectively.

$$\text{E.R.} = \frac{m}{S_t}$$

$$\eta = \frac{mh_{LV}}{qC_{opt}}$$

We calculated its evaporation rate for bulk water is t 0.35 kg/m^2/h and its evaporation efficiency is 22.32%. The floating structure is slightly improved compared to the bulk water sample the evaporation rate and efficiency are 0.53 kg/m^2/h and 33.76% respectively. (The confined heating evaporator has a huge improvement compared to the floating structure. The confined heating evaporators of different thicknesses (2 mm, 4 mm, 6 mm) have different evaporation rates of 1.05 kg/m^2/h 1.49 kg/m^2/h and 1.29 kg/m^2/h respectively. Their evaporation efficiencies are 64.60%, 91.68%, and 79.37% respectively. Compared with the 6 mm water layer, the 4 mm water layer has a faster heating rate and less heat loss, so it has a better evaporation rate and efficiency. However, further reducing the thickness of the water layer will not only make the preparation process more difficult, and the actual evaporation

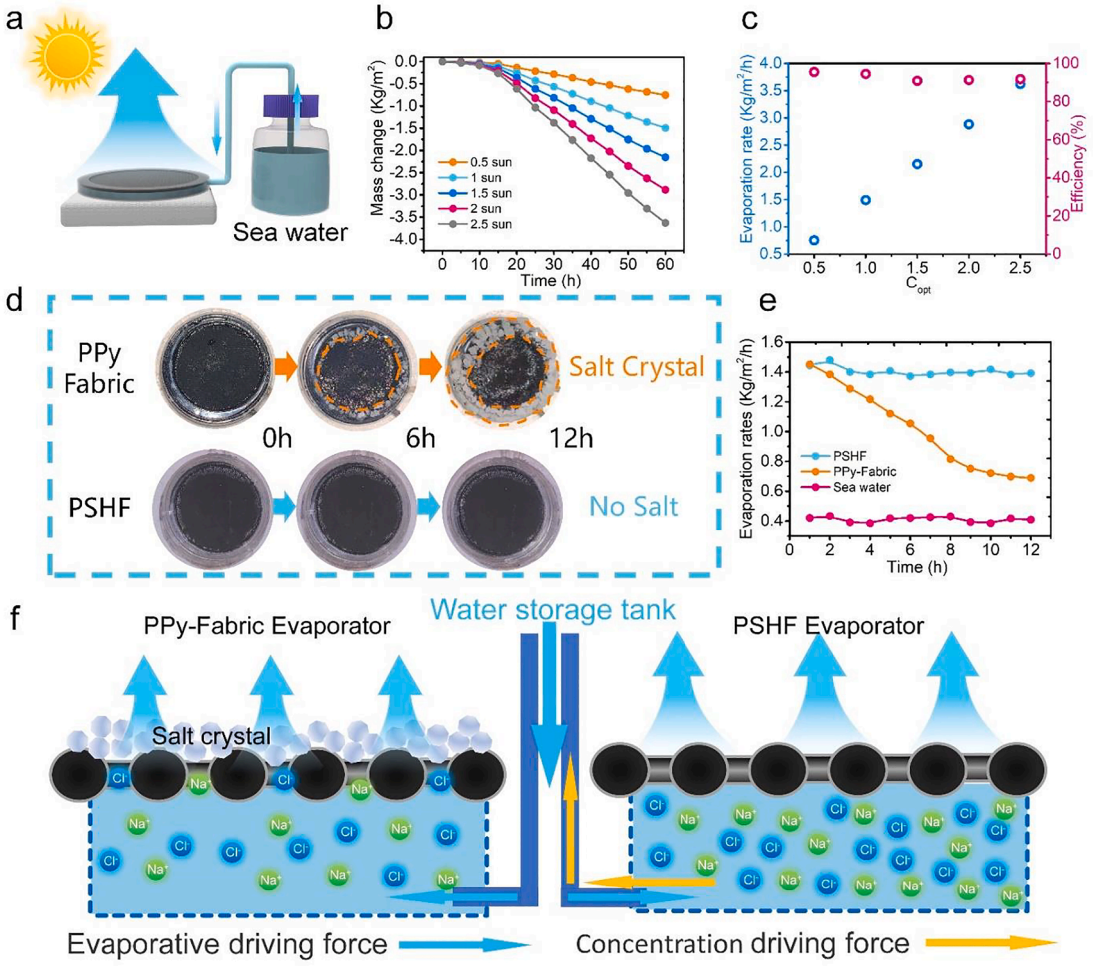

Fig. 5. (a) Sketch of the confined heating evaporator with simulative sunlight in the laboratory. (b) Mass change versus time curves of confined heating evaporator under different optical concentrations. (c) Evaporation rate and efficiency of the confined heating evaporator under different optical concentrations. (d) Photos of the confined heating evaporators loaded with PPy Fabric and PSHF evaporate for 12 h in seawater. (e) Evaporation rates of seawater, confined heating evaporators with PPy Fabric and PSHF surface.

rate may be hardly increased or even decreased. Therefore, we finally use the confined heating evaporator with the water layer thickness of 4 mm for further study.

It is worth noting that, different from the mass loss curve of bulk water and conventional floating structure present a linear curve, the confined heating evaporators have a non-linear mass loss curve from 0 to 60 min (Fig. 4g and 4 h). As for the confined heating evaporator with a thickness of 4 mm water layer. Among them, because the temperature didn't reach the highest, the mass loss is little within 0–20 min. After 20 min, due to the temperature of the water layer in the evaporator had reached the highest level, the mass loss of these evaporators had a sudden rise. After 20 min, the data line of mass loss tends to the straight. This rule of the curve is consistent with the previous temperature increase regularly. Because the temperature of the surface and internal water layer of the evaporator has reached a balance after 20 min. When the temperature continues to rise, the mass loss of water per unit of time will also become stable.

For the solar-driven evaporation application, quantitative experiments were conducted to investigate the evaporation performance using a solar simulator-based apparatus (Fig. 5a). To further investigate the capability of the solar evaporator performance under different light intensities, the relative mass change curves under different light intensity from 0.5 to 2.5 sun are recorded and shown in Fig. 5b. The results demonstrated that there is a positive correlation between evaporation rates and light intensity, ranging from 0.7 to 3.623 kg/m^2, which ensured good adaptability in changeable environments. At the same time, the efficiency was also calculated, but it does not have certain correlation with the evaporation rates (Fig. 5c). The results show that the confined heating evaporator has good photothermal evaporative capacity under different intensity of sunlight. As shown in Fig S16, compared with the seawater exposure under 1 sun irradiation directly for evaporation (0.38 kg/m^2/h), the confined heating evaporator has a similar evaporation rate in both pure water and seawater, which can reach about 1.49 kg/m^2/h. Furthermore, in order to verify the reuse properties of materials, we repeated 10 cycles of the PSHF evaporator under 1 sun irradiation in brine. As shown in Fig. S17. In 10 experiments, the results fluctuated around 1.5 kg/m^2/h, which proves that this evaporator has the tremendous potential of reuse in the actual application of solar driven evaporation.

Since the evaporated durability in brine is a critical factor for the solar evaporators, salt-resistance evaporation experiments are conducted in our system. The long-term evaporation performance of the confined heating evaporator loaded with PPy Fabric and PSHF were tested respectively in simulated seawater (3.6 wt% NaCl solution) for 12 h. As shown in Fig. 5d. The results show that during the long-term evaporation process in simulated seawater, a lot of salt gradually accumulated on the surface of the evaporator loaded with the PPy Fabric photothermal layer. However, due to the superhydrophobic property of PSHF, it cannot be permeated by water during the long-term evaporation process, so the surface of the evaporator loaded with PSHF

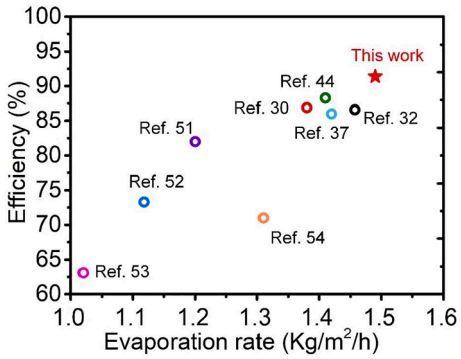

Fig. 6. The comparison of efficiency and evaporation rate for different solar-driven evaporator based on superhydrophobic surface previously reported.

photothermal layer has no obvious change. Through the statistical calculation of the evaporation rate, because of the accumulation of salt, the evaporation rate of the PPy Fabric evaporator decreases gradually over time, but the PSHF evaporator still keeps stable. (Fig. 5e).

As shown in Fig. 5f, we further analyse the mechanism of both kinds of evaporators. First of all, the ions and water molecules in the simulated seawater are constantly taken to the photothermal layer by the evaporation driving force the in PPy fabric evaporator system. Then the liquid water is evaporated and leave the salt crystal on the photothermal surface. The PSHF evaporator can prevent ions from infiltrating with the surface of the photothermal layer, which makes the ions concentration in the PSHF evaporator increase gradually. A certain concentration difference will form between the seawater in the evaporation system with the water storage tank. Ions may be constantly moving from a high concentration area to a low concentration area utilizing concentration differences.

In order to prove this guess, the internal water ions concentration of PPy-fabric and PSHF evaporators were analysed by inductively coupled plasma mass spectrometry. The results showed that the ions concentration in the evaporator PPy-fabric remained below 3.5 wt% after 12 h evaporation. This is mainly because of the continuous crystallization of salt on the surface of the PPy-fabric evaporator. However, the PSHF photothermal layer has strong resistance to seawater. Salt can't be removed by crystallization. The results showed that the ions concentration in the PSHF evaporator increase slightly and concentrate to about 4.2%. But this concentration is still much lower than that of saturated NaCl solution (26.5 wt%). The guess has been proved that the movement of the ions due to the concentration difference exists between the PSHF evaporator with the water storage tank. Therefore, the confined heating evaporator loaded with PSHF has long-term stability in the brine environment.

As shown in Fig. 6 and Tab. 3, we also compare the previous work of solar energy driven using superhydrophobic interface structure. Such as hydrophobic/hydrophilic graphene foams[30], carbon black polyacrylonitrile (CB/PAN) composite nanofiber[46], silver nanoparticles graphite modified sponge[58], hydrophilic/hydrophobic nanoporous double layer[32] superhydrophilic porous monolithic polymer foam [44], superhydrophilic porous carbon foam[37], PVDF membranes[59] and 2D Ti_3C_2 MXene membrane[60]

To investigate the solar desalination capability of the confined heating evaporator in the true environment. As shown in Fig. 7a, steam was generated continuously from the surface of the evaporator and a sealed chamber was design for collecting distilled water. The bottle for storing seawater is placed outside the sealed chamber, and the water is delivered through a soft tube. When the whole device is placed in outdoor sunlight, as shown in the photos of Fig. 7b, the steam will quickly condense on the surface of the sealer within 1 h. The diameter of the evaporator used in the outdoor experiment is 5 cm. By comparing the evaporator before and after evaporation, no obvious salt crystallization was found, which proves that it has excellent stability in the actual environment. (Fig. 7c). The outdoor experiment was conducted from 9:00 to 17:00 under natural sunlight with an average solar heat flux of 916.33 w/m^2. The average evaporation rate of this day can be calculated as 1.12 kg/m^2. As displayed in Fig. 7d, based on the analysis of

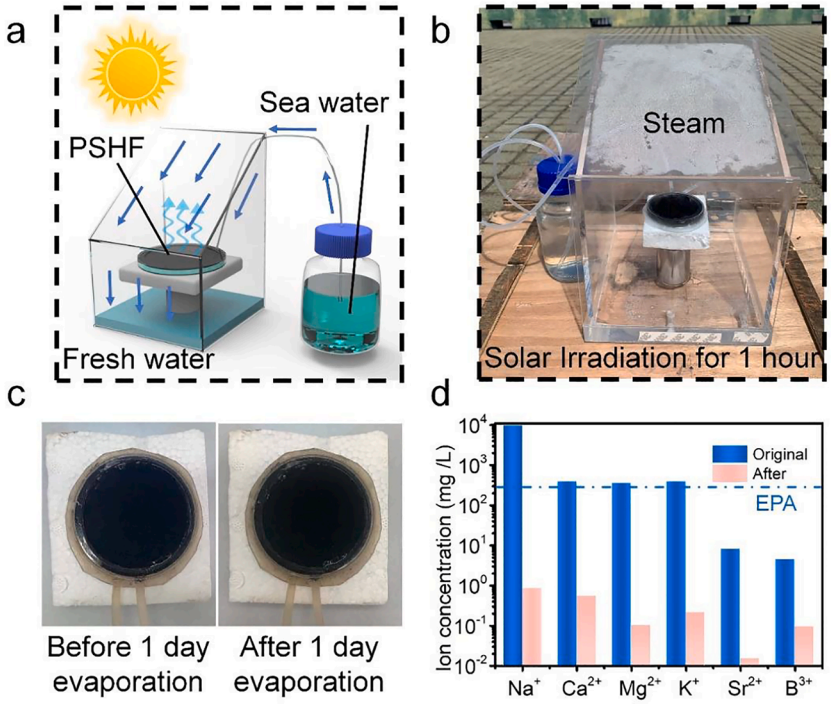

Fig. 7. (a) Schematic of the confined heating evaporation and water collection system with actual sunlight in outdoor. (b) Photograph of confined heating evaporation device in sealed chambers after 1 h. Solar steam quickly coagulates in the inner wall of the sealed chambers. (c) Photograph of confined heating evaporation device in sealed chambers under natural sunlight. (d) The measured ion concentration of six simulated seawater samples before and after desalination.

inductively-coupled plasma mass spectrometry, the concentrations of four primary ions in the condensed water, including Na^+, Mg^{2+}, Ca^{2+}, K^+, Sr^{2+} and B^{3+}, were all reduced by over three orders of magnitude as compared with the initial concentrations of the artificial seawater. The resultant salinity level well complied with the standard for healthy drinking water, that defined by the US Environmental Protection Agency (EPA).[61]

4. Conclusions

In summary, we have demonstrated a solar-driven confined heating strategy. Efficient and sustainable seawater purification is achieved by a self-closing photothermal breathable "cover". This "cover" consists of a photothermal conversion, breathable and superhydrophobic PSHF, which can be prepared in a simple way over a large area. The confined heating evaporator load with PSHF allows for efficient energy management by reducing heat conduction losses. Note that when the thickness of the evaporator is optimized to 4 mm, the heat conduction can reduce to 0.98%, and the total heat loss is only 7.1%. The surface temperature of PSHF confined strategy can reach to 59.7 °C is 14.9 °C higher than the conventional strategy (45.8 °C). The evaporation rate can be optimized to 1.49 kg/m^2/h, and the evaporation efficiency is 91.68% under 1 sun irradiation (1 kW/m^2). At the same time, superhydrophobic properties of the photothermal layer can also endow the evaporators with good salt rejection performance. It can remain stable under the long-term evaporation of 12 h. The results indicate that the superhydrophobic confined heating system is reliable for efficient and sustainable seawater desalination, demonstrating significant potentials in sustainable water purification.

Declaration of Competing Interest

The authors declare that they have no known competing financial interests or personal relationships that could have appeared to influence the work reported in this paper.

Acknowledgements

We thank the Natural Science Foundation of China (51803226), Key Research Program of Frontier Sciences, Chinese Academy of Sciences (QYZDB-SSWSLH036), Bureau of International Cooperation of Chinese Academy of Sciences (174433KYSB20170061), Postdoctoral Innovation Talent Support Program (BX20180321), K. C. Wong Education Foundation (GJTD-2019-13).

Appendix A. Supplementary data

Supplementary data to this article can be found online at https://doi.org/10.1016/j.cej.2021.131142.

References:

[1] M. Elimelech, W.A. Phillip, The future of seawater desalination: energy, technology, and the environment, Science 333 (6043) (2011) 712–717, https://doi.org/10.1126/science.1200488.
[2] J. Eliasson, The rising pressure of global water shortages, Nature 517 (7532) (2015) 6–7, https://doi.org/10.1038/517006a.
[3] C. Chen, Y. Kuang, L. Hu, Challenges and Opportunities for Solar Evaporation, Joule 3 (3) (2019) 683–718, https://doi.org/10.1016/j.joule.2018.12.023.
[4] V.-D. Dao, N.H. Vu, S. Yun, Recent advances and challenges for solar-driven water evaporation system toward applications, Nano Energy 68 (2020) 104324, https://doi.org/10.1016/j.nanoen.2019.104324.
[5] S.-L. Wu, H. Chen, H.-L. Wang, X. Chen, H.-C. Yang, S.B. Darling, Solar-driven evaporators for water treatment: challenges and opportunities, Environ. Sci. Wat. Res. 7 (1) (2021) 24–39, https://doi.org/10.1039/D0EW00725K.
[6] M. Gao, L. Zhu, C.K. Peh, G.W. Ho, Solar absorber material and system designs for photothermal water vaporization towards clean water and energy production, Energy Environ. Sci. 12 (3) (2019) 841–864, https://doi.org/10.1039/c8ee01146j.
[7] F. Ni, P. Xiao, N. Qiu, C. Zhang, Y. Liang, J. Gu, J. Xia, Z. Zeng, L. Wang, Q. Xue, T. Chen, Collective behaviors mediated multifunctional black sand aggregate towards environmentally adaptive solar-to-thermal purified water harvesting, Nano Energy 68 (2020) 104311, https://doi.org/10.1016/j.nanoen.2019.104311.
[8] P. Tao, G. Ni, C. Song, W. Shang, J. Wu, J. Zhu, G. Chen, T. Deng, Solar-driven interfacial evaporation, Nat. Energy 3 (12) (2018) 1031–1041, https://doi.org/10.1038/s41560-018-0260-7.
[9] L. Zhu, T. Ding, M. Gao, C.K.N. Peh, G.W. Ho, Shape Conformal and Thermal Insulative Organic Solar Absorber Sponge for Photothermal Water Evaporation and Thermoelectric Power Generation, Adv. Energy Mater. 9 (22) (2019) 1900250, https://doi.org/10.1002/aenm.v9.2210.1002/aenm.201900250.
[10] P. Mu, Z. Zhang, W. Bai, J. He, H. Sun, Z. Zhu, W. Liang, A.n. Li, Superwetting Monolithic Hollow-Carbon-Nanotubes Aerogels with Hierarchically Nanoporous Structure for Efficient Solar Steam Generation, Adv. Energy Mater. 9 (1) (2019) 1802158, https://doi.org/10.1002/aenm.v9.110.1002/aenm.201802158.
[11] P. Xiao, J. He, Y. Liang, C. Zhang, J. Gu, J. Zhang, Y. Huang, S.-W. Kuo, T. Chen, Rationally Programmable Paper-Based Artificial Trees Toward Multipath Solar-Driven Water Extraction from Liquid/Solid Substrates, Solar RRL 3 (7) (2019) 1900004, https://doi.org/10.1002/solr.v3.710.1002/solr.201900004.
[12] F. Ni, P. Xiao, C. Zhang, Y. Liang, J. Gu, L. Zhang, T. Chen, Micro-/Macroscopically Synergetic Control of Switchable 2D/3D Photothermal Water Purification Enabled by Robust, Portable, and Cost-Effective Cellulose Papers, ACS Appl Mater Interfaces 11 (17) (2019) 15498–15506, https://doi.org/10.1021/acsami.9b0038010.1021/acsami.9b00380.s001.
[13] K. Li, T.-H. Chang, Z. Li, H. Yang, F. Fu, T. Li, J.S. Ho, P.-Y. Chen, Biomimetic MXene Textures with Enhanced Light-to-Heat Conversion for Solar Steam Generation and Wearable Thermal Management, Adv. Energy Mater. 9 (34) (2019) 1901687, https://doi.org/10.1002/aenm.v9.3410.1002/aenm.201901687.
[14] Z. Zhang, Y. Wang, P.A. Stensby Hansen, K. Du, K.R. Gustavsen, G. Liu, F. Karlsen, O. Nilsen, C. Xue, K. Wang, Black silicon with order-disordered structures for enhanced light trapping and photothermic conversion, Nano Energy 65 (2019) 103992, https://doi.org/10.1016/j.nanoen.2019.103992.
[15] L. Zhao, B. Bhatia, L. Zhang, E. Strobach, A. Leroy, M.K. Yadav, S. Yang, T. A. Cooper, L.A. Weinstein, A. Modi, S.B. Kedare, G. Chen, E.N. Wang, A Passive High-Temperature High-Pressure Solar Steam Generator for Medical Sterilization, Joule 4 (12) (2020) 2733–2745, https://doi.org/10.1016/j.joule.2020.10.007.
[16] J. Chen, D. Zhang, S. He, G. Xia, X. Wang, Q. Xiang, T. Wen, Z. Zhong, Y. Liao, Thermal insulation design for efficient and scalable solar water interfacial evaporation and purification, J. Mater. Sci. Technol. 66 (2021) 157–162, https://doi.org/10.1016/j.jmst.2020.05.075.
[17] Y. Wang, X. Wu, X. Yang, G. Owens, H. Xu, Reversing heat conduction loss: Extracting energy from bulk water to enhance solar steam generation, Nano Energy 78 (2020) 105269, https://doi.org/10.1016/j.nanoen.2020.105269.
[18] A.K. Menon, I. Haechler, S. Kaur, S. Lubner, R.S. Prasher, Enhanced solar evaporation using a photo-thermal umbrella for wastewater management, Nat. Sustain. 3 (2) (2020) 144–151, https://doi.org/10.1038/s41893-019-0445-5.
[19] Q.-F. Guan, Z.-M. Han, Z.-C. Ling, H.-B. Yang, S.-H. Yu, Sustainable Wood-Based Hierarchical Solar Steam Generator: A Biomimetic Design with Reduced Vaporization Enthalpy of Water, Nano Lett 20 (8) (2020) 5699–5704, https://doi.org/10.1021/acs.nanolett.0c0108810.1021/acs.nanolett.0c01088.s001.
[20] T. Li, H.e. Liu, X. Zhao, G. Chen, J. Dai, G. Pastel, C. Jia, C. Chen, E. Hitz, D. Siddhartha, R. Yang, L. Hu, Scalable and Highly Efficient Mesoporous Wood-Based Solar Steam Generation Device: Localized Heat, Rapid Water Transport, Adv. Funct. Mater. 28 (16) (2018) 1707134, https://doi.org/10.1002/adfm.v28.1610.1002/adfm.201707134.
[21] J. Tang, T. Zheng, Z. Song, Y. Shao, N. Li, K. Jia, Y. Tian, Q. Song, H. Liu, G. Xue, Realization of Low Latent Heat of a Solar Evaporator via Regulating the Water State in Wood Channels, ACS Appl. Mater. Interfaces 12 (16) (2020) 18504–18511, https://doi.org/10.1021/acsami.0c0126110.1021/acsami.0c01261.s001.
[22] S. He, C. Chen, Y. Kuang, R. Mi, Y. Liu, Y. Pei, W. Kong, W. Gan, H. Xie, E. Hitz, C. Jia, X. Chen, A. Gong, J. Liao, J. Li, Z.J. Ren, B. Yang, S. Das, L. Hu, Nature-inspired salt resistant bimodal porous solar evaporator for efficient and stable water desalination, Energy Environ. Sci. 12 (5) (2019) 1558–1567, https://doi.org/10.1039/c9ee00945k.
[23] G. Ni, S.H. Zandavi, S.M. Javid, S.V. Boriskina, T.A. Cooper, G. Chen, A salt-rejecting floating solar still for low-cost desalination, Energy Environ. Sci. 11 (6) (2018) 1510–1519, https://doi.org/10.1039/c8ee00220g.
[24] L. Huang, L.i. Ling, J. Su, Y. Song, Z. Wang, B.Z. Tang, P. Westerhoff, R. Ye, Laser-Engineered Graphene on Wood Enables Efficient Antibacterial, Anti-Salt-Fouling, and Lipophilic-Matter-Rejection Solar Evaporation, ACS Appl. Mater. Interfaces 12 (46) (2020) 51864–51872, https://doi.org/10.1021/acsami.0c1659610.1021/acsami.0c16596.s001.
[25] S. Wu, G. Xiong, H. Yang, B. Gong, Y. Tian, C. Xu, Y. Wang, T. Fisher, J. Yan, K. Cen, T. Luo, X. Tu, Z. Bo, K.(. Ostrikov, Multifunctional Solar Waterways: Plasma-Enabled Self-Cleaning Nanoarchitectures for Energy-Efficient Desalination, Adv. Energy Mater. 9 (30) (2019) 1901286, https://doi.org/10.1002/aenm.v9.3010.1002/aenm.201901286.
[26] Z. Wang, M. Han, F. He, S. Peng, S.B. Darling, Y. Li, Versatile coating with multifunctional performance for solar steam generation, Nano Energy 74 (2020) 104886, https://doi.org/10.1016/j.nanoen.2020.104886.
[27] S.K. Patel, C.L. Ritt, A. Deshmukh, Z. Wang, M. Qin, R. Epsztein, M. Elimelech, The relative insignificance of advanced materials in enhancing the energy efficiency of desalination technologies, Energy Environ. Sci. 13 (6) (2020) 1694–1710, https://doi.org/10.1039/d0ee00341g.
[28] F. Zhao, Y. Guo, X. Zhou, W. Shi, G. Yu, Materials for solar-powered water evaporation, Nat. Rev. Mater. 5 (5) (2020) 388–401, https://doi.org/10.1038/s41578-020-0182-4.

[29] Y. Zhang, T. Xiong, D.K. Nandakumar, S.C. Tan, Structure Architecting for Salt-Rejecting Solar Interfacial Desalination to Achieve High-Performance Evaporation With In Situ Energy Generation, Adv. Sci. 7 (9) (2020) 1903478, https://doi.org/10.1002/advs.v7.910.1002/advs.201903478.
[30] J. Chen, J.L. Yin, B.o. Li, Z. Ye, D. Liu, D. Ding, F. Qian, N.V. Myung, Q. Zhang, Y. Yin, Janus Evaporators with Self-Recovering Hydrophobicity for Salt-Rejecting Interfacial Solar Desalination, ACS Nano 14 (12) (2020) 17419–17427, https://doi.org/10.1021/acsnano.0c0767710.1021/acsnano.0c07677.s00110.1021/acsnano.0c07677.s00210.1021/acsnano.0c07677.s00310.1021/acsnano.0c07677.s004.
[31] Q.i. Zhang, G. Yi, Z.e. Fu, H. Yu, S. Chen, X. Quan, Vertically Aligned Janus MXene-Based Aerogels for Solar Desalination with High Efficiency and Salt Resistance, ACS Nano 13 (11) (2019) 13196–13207, https://doi.org/10.1021/acsnano.9b0618010.1021/acsnano.9b06180.s001.
[32] Y. Yang, H. Zhao, Z. Yin, J. Zhao, X. Yin, N. Li, D. Yin, Y. Li, B. Lei, Y. Du, W. Que, A general salt-resistant hydrophilic/hydrophobic nanoporous double layer design for efficient and stable solar water evaporation distillation, Mater. Horiz. 5 (6) (2018) 1143–1150, https://doi.org/10.1039/c8mh00386f.
[33] D.D. Qin, Y.J. Zhu, R.L. Yang, Z.C. Xiong, A salt-resistant Janus evaporator assembled from ultralong hydroxyapatite nanowires and nickel oxide for efficient and recyclable solar desalination, Nanoscale 12 (12) (2020) 6717–6728, https://doi.org/10.1039/c9nr10357k.
[34] Y. Liu, J. Chen, D. Guo, M. Cao, L. Jiang, Floatable, Self-Cleaning, and Carbon-Black-Based Superhydrophobic Gauze for the Solar Evaporation Enhancement at the Air-Water Interface, ACS Appl. Mater. Interfaces 7 (24) (2015) 13645–13652, https://doi.org/10.1021/acsami.5b03435.
[35] X. Zhang, Y. Peng, L. Shi, R. Ran, Highly Efficient Solar Evaporator Based On a Hydrophobic Association Hydrogel, ACS Sustain. Chem. Eng. 8 (49) (2020) 18114–18125, https://doi.org/10.1021/acssuschemeng.0c06462.
[36] F. Liu, W. Liang, C. Wang, C. Xiao, J. He, G. Zhao, Z. Zhu, H. Sun, A.n. Li, Superhydrophilic and mechanically robust phenolic resin as double layered photothermal materials for efficient solar steam generation, Mater. Today Energy 16 (2020) 100375, https://doi.org/10.1016/j.mtener.2019.100375.
[37] C. Wang, J. Wang, Z. Li, K. Xu, T. Lei, W. Wang, Superhydrophilic porous carbon foam as a self-desalting monolithic solar steam generation device with high energy efficiency, J. Mater. Chem. A 8 (19) (2020) 9528–9535, https://doi.org/10.1039/d0ta01439g.
[38] L. Wu, Z. Dong, Z. Cai, T. Ganapathy, N.X. Fang, C. Li, C. Yu, Y. Zhang, Y. Song, Highly efficient three-dimensional solar evaporator for high salinity desalination by localized crystallization, Nat. Commun. 11 (1) (2020) 521, https://doi.org/10.1038/s41467-020-14366-1.
[39] S.C. Singh, M. ElKabbash, Z. Li, X. Li, B. Regmi, M. Madsen, S.A. Jalil, Z. Zhan, J. Zhang, C. Guo, Solar-trackable super-wicking black metal panel for photothermal water sanitation, Nat. Sustain. 3 (11) (2020) 938–946, https://doi.org/10.1038/s41893-020-0566-x.
[40] M. Morciano, M. Fasano, S.V. Boriskina, E. Chiavazzo, P. Asinari, Solar passive distiller with high productivity and Marangoni effect-driven salt rejection, Energy Environ. Sci. 13 (10) (2020) 3646–3655, https://doi.org/10.1039/D0EE01440K.
[41] Y. Xia, Q. Hou, H. Jubaer, Y. Li, Y. Kang, S. Yuan, H. Liu, M.W. Woo, L. Zhang, L. Gao, H. Wang, X. Zhang, Spatially isolating salt crystallisation from water evaporation for continuous solar steam generation and salt harvesting, Energy Environ. Sci. 12 (6) (2019) 1840–1847, https://doi.org/10.1039/c9ee00692c.
[42] Z. Liu, B. Wu, B.o. Zhu, Z. Chen, M. Zhu, X. Liu, Continuously Producing Watersteam and Concentrated Brine from Seawater by Hanging Photothermal Fabrics under Sunlight, Adv. Funct. Mater. 29 (43) (2019) 1905485, https://doi.org/10.1002/adfm.v29.4310.1002/adfm.201905485.
[43] L. Zhao, L. Wang, J. Shi, X. Hou, Q.i. Wang, Y. Zhang, Y. Wang, N. Bai, J. Yang, J. Zhang, B.o. Yu, C.F. Guo, Shape-Programmable Interfacial Solar Evaporator with Salt-Precipitation Monitoring Function, ACS Nano 15 (3) (2021) 5752–5761, https://doi.org/10.1021/acsnano.1c0129410.1021/acsnano.1c01294.s00110.1021/acsnano.1c01294.s002.
[44] J. He, Z. Zhang, C. Xiao, F. Liu, H. Sun, Z. Zhu, W. Liang, A.n. Li, High-Performance Salt-Rejecting and Cost-Effective Superhydrophilic Porous Monolithic Polymer Foam for Solar Steam Generation, ACS Appl. Mater. Interfaces 12 (14) (2020) 16308–16318, https://doi.org/10.1021/acsami.9b2283210.1021/acsami.9b22832.s001.
[45] X. Wu, L. Wu, J. Tan, G.Y. Chen, G. Owens, H. Xu, Evaporation above a bulk water surface using an oil lamp inspired highly efficient solar-steam generation strategy, J. Mater. Chem. A 6 (26) (2018) 12267–12274, https://doi.org/10.1039/c8ta03280g.
[46] T. Gao, Y. Li, C. Chen, Z. Yang, Y. Kuang, C. Jia, J. Song, E.M. Hitz, B. Liu, H. Huang, J. Yu, B. Yang, L. Hu, Architecting a Floatable, Durable, and Scalable Steam Generator: Hydrophobic/Hydrophilic Bifunctional Structure for Solar Evaporation Enhancement, Small Methods 3 (2) (2019) 1800176, https://doi.org/10.1002/smtd.v3.210.1002/smtd.201800176.
[47] C.-S. Hu, H.-J. Li, J.-Y. Wang, A. Haleem, X.-C. Li, M. Siddiq, W.-D. He, Mushroom-Like rGO/PAM Hybrid Cryogels with Efficient Solar-Heating Water Evaporation, ACS Appl. Mater. Interfaces 2 (10) (2019) 7554–7563, https://doi.org/10.1021/acsaem.9b0153010.1021/acsaem.9b01530.s001.
[48] X. Ma, Z. Li, Z. Deng, D. Chen, X. Wang, X. Wan, Z. Fang, X. Peng, Efficiently cogenerating drinkable water and electricity from seawater via flexible MOF nanorod arrays, J. Mater. Chem. A 9 (14) (2021) 9048–9055, https://doi.org/10.1039/d0ta11870b.
[49] T.A. Cooper, S.H. Zandavi, G.W. Ni, Y. Tsurimaki, Y. Huang, S.V. Boriskina, G. Chen, Contactless steam generation and superheating under one sun illumination, Nat Commun 9 (1) (2018) 5086, https://doi.org/10.1038/s41467-018-07494-2.
[50] S. Cao, Q. Jiang, X. Wu, D. Ghim, H. Gholami Derami, P.-I. Chou, Y.-S. Jun, S. Singamaneni, Advances in solar evaporator materials for freshwater generation, J. Mater. Chem.A 7 (42) (2019) 24092–24123.
[51] A. Utgenannt, R. Maspero, A. Fortini, R. Turner, M. Florescu, C. Jeynes, A. G. Kanaras, O.L. Muskens, R.P. Sear, J.L. Keddie, Fast Assembly of Gold Nanoparticles in Large-Area 2D Nanogrids Using a One-Step, Near-Infrared Radiation-Assisted Evaporation Process, ACS Nano 10 (2) (2016) 2232–2242, https://doi.org/10.1021/acsnano.5b06886.
[52] M.A. Raza, E.S. Kooij, A. Silfhout, B. Poelsema, Superhydrophobicity of Self-Assembled PFDTS Nanostructures, Progr, Colloid. Polym. Sci. (2011) 81–84, https://doi.org/10.1007/978-3-642-19038-4_14.
[53] J.L. Ning Xu, Yang Wang, Chang Fang, Xiuqiang Li, Yuxi Wang, Lin Zhou, Bin Zhu, Zhen Wu, Shining Zhu, Jia Zhu, A water lily–inspired hierarchical design for stable and efficient solar evaporation of high-salinity brine, Sci. Adv. 5 (2019) 7013.
[54] R.N. Wenzel, Resistance of Solid Surfaces to Wetting by Water, Ind. Eng. Chem. 28 (8) (1936) 988–994.
[55] A.B.D. Cassie, S. Baxter, Wettability of porous surfaces, Transactions of the Faraday Society 40 (1944) 546, https://doi.org/10.1039/tf9444000546.
[56] S. Wang, L. Jiang, Definition of Superhydrophobic States, Adv. Mater. 19 (21) (2007) 3423–3424, https://doi.org/10.1002/(ISSN)1521-409510.1002/adma.v19:2110.1002/adma.200700934.
[57] L. Zhang, B.o. Tang, J. Wu, R. Li, P. Wang, Hydrophobic Light-to-Heat Conversion Membranes with Self-Healing Ability for Interfacial Solar Heating, Adv. Mater. 27 (33) (2015) 4889–4894, https://doi.org/10.1002/adma.v27.3310.1002/adma.201502362.
[58] Z. Zhang, P. Mu, J. He, Z. Zhu, H. Sun, H. Wei, W. Liang, A.n. Li, Facile and Scalable Fabrication of Surface-Modified Sponge for Efficient Solar Steam Generation, ChemSusChem 12 (2) (2019) 426–433, https://doi.org/10.1002/cssc.v12.210.1002/cssc.201802406.
[59] T. Li, Q. Fang, H. Lin, F. Liu, Enhancing solar steam generation through manipulating the heterostructure of PVDF membranes with reduced reflection and conduction, J. Mater. Chem. A 7 (29) (2019) 17505–17515, https://doi.org/10.1039/c9ta03865e.
[60] J. Zhao, Y. Yang, C. Yang, Y. Tian, Y. Han, J. Liu, X. Yin, W. Que, Yan Han, Jie Liu, Xingtian Yin and Wenxiu Que, A hydrophobic surface enabled salt-blocking 2D Ti_3C_2 MXene membrane for efficient and stable solar desalination, J. Mater. Chem. A 6 (33) (2018) 16196–16204, https://doi.org/10.1039/C8TA05569F.
[61] L. Zhu, L. Sun, H. Zhang, H. Aslan, Y.e. Sun, Y. Huang, F. Rosei, M. Yu, A solution to break the salt barrier for high-rate sustainable solar desalination, Energy Environ. Sci. 14 (4) (2021) 2451–2459, https://doi.org/10.1039/D1EE00113B.